Supporting Online Material: Eddy-driven stratification initiates a North Atlantic Spring phytoplankton bloom

Amala Mahadevan,[1] Eric D'Asaro,[2*] Craig Lee,[2] Mary Jane Perry[3]

[1]Woods Hole Oceanographic Institution, Woods Hole, MA 02543, USA
[2]Applied Ocean Physics Laboratory, University of Washington, Seattle, WA 98195, USA
[3]Darling Marine Center, University of Maine, Walpole, ME 04573, USA
* Eric D'Asaro; E-mail: dasaro@apl.washington.edu

November 28, 2012

1 Methods and Materials

1.1 Seagliders

Seagliders are small (1.2m, 52 kg) autonomous vehicles that fly horizontally at $0.2\mathrm{ms}^{-1}$ through the ocean driven by their own buoyancy (*1*). Four Seagliders (SG140, SG141, SG142, and SG143) surveyed in a 50-100 km-wide region around the float throughout its deployment (Fig. S1, blue) and then surveyed until June 28 over the flanks of the Reykjanes Ridge. Seagliders dove to 1000 m about four times per day while measuring temperature, salinity, chlorophyll and other quantities (Fig. S2). Seagliders communicated via Iridium during the 15-minute surfacing window between dive cycles, thus allowing them to be steered in relation to the float's last known position, or a predicted future position based on previous behavior.

1.2 Lagrangian Float

The Lagrangian float, serial number 48, was built at the University of Washington, Applied Physics Laboratory and is similar to those described in D'Asaro (2003) (*2*). It is about 1.4 m long with a displacement of about 59 L. Unlike ARGO floats, which are designed to efficiently profile, it is primarily designed to accurately follow the three-dimensional motion of water parcels within the mixed layer (ML), through a combination of neutral buoyancy and high

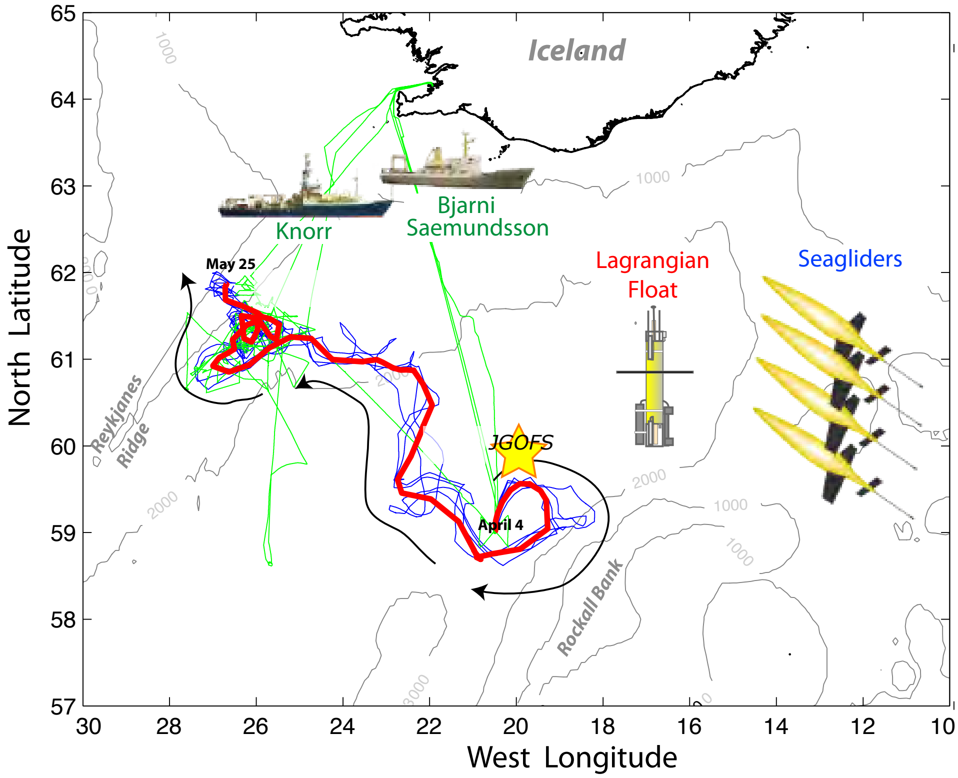

Figure S1: Map of NAB08 Data. The tracks of Float 48 drift (red), Seagliders (blue), and supporting cruises (green) of the *R/V Knorr* and *R/V Bjarni Saemundsson* are plotted as colored lines. The direction of the float drift, beginning April 4 and ending May 25, is illustrated using black arrows. The location of the JGOFS 1989 North Atlantic Bloom Experiment is plotted as a yellow star for reference.

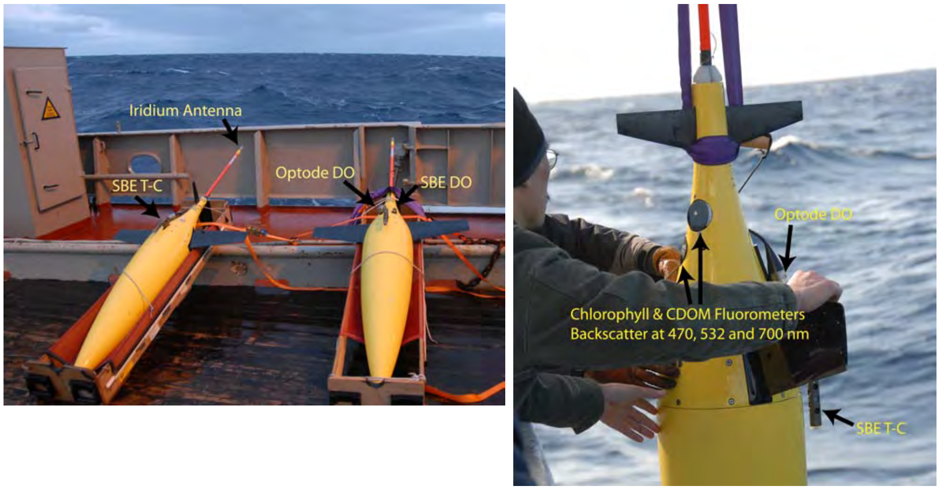

Figure S2: Seagliders used in NAB08 showing location of sensors.

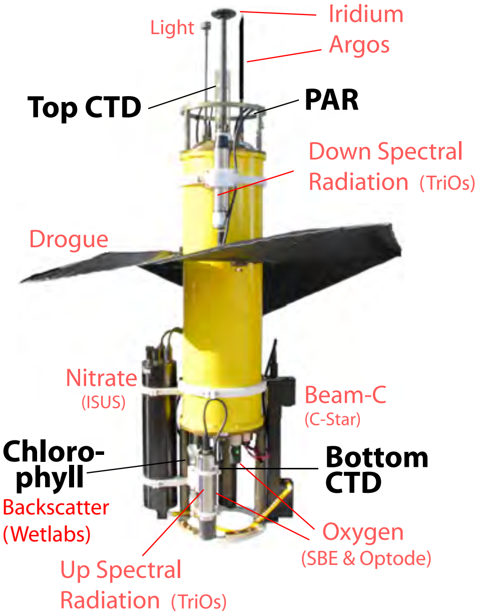

Figure S3: Lagrangian Float configured for the NAB08 measurements. Sensors used in this analysis are labelled in black, others in dimmed red. The drogue (black) normally rests perpendicular to the float hull when it is open.

drag provided by a 1 m-diameter drogue. The float does not exactly match the density of the surrounding water, resulting in a net buoyancy force of a few grams and resulting in vertical velocities relative to the water of a few millimeters per second, small compared to the centimeter per second turbulent velocities in the ML. The float's motion within the ML thus closely imitates that of a Lagrangian trajectory. The float can also profile vertically and send data and receive commands using the Iridium satellite system. The NAB08 float carried a heavy load of sensors; those relevant to this analysis are described below.

The Lagrangian float executed a daily mission cycle. During most of the day, the float drifted in the ML and was repeatedly carried across the region of active mixing by the boundary layer turbulence. Once per day, typically near 15 UTC, the float surfaced and communicated using Iridium, then profiled to about 230 m, conducted an auto-ballasting operation, profiled back to the surface, and resumed drifting in the ML. The float collected data in all operational modes (except during communications) sampling temperature, salinity and chlorophyll on a 50-60 s interval. The daily downcasts comprised 21% of the total available data collected by the float. In contrast, the ML drifts provided 56% of the available data but were limited to shallow depths (75% of drift mode data restricted to $<$ 20 m). The remaining 23% of the data was collected during upcast and autoballasting modes.

1.3 Sensor Calibration

A series of calibration casts were made by the ships close to the float and Seagliders, typically closer than 1 km, in order to provide accurate CTD and bottle data for sensor calibration. In addition, many opportunities for cross-calibration of the autonomous sensors occurred as Seagliders passed close to other Seagliders or the float. A series of reports describing the calibration and performance of the ship, float, and Seaglider sensors, along with the data from these sensors is available online at the Biological and Chemical Oceanography Data Management Office: `http://osprey.bcodmo.org/project.cfm?flag=view&id=102&sortby=project`. Key results from these reports are summarized below.

The CTD sensors on both floats, the Knorr cruise, the float deployment cruise on the *Bjarni Saemundsson* and the pre- and post-cruise float sensor calibrations were compared. Formulae were found to bring them all into agreement to within 0.001 in both salinity (psu) and temperature (C) using the Knorr CTD as the absolute standard. An algorithm to merge data from the two float CTDs into a single time series is used to reduce the effect of a variety of small errors.

Seagliders SG140, SG141 and SG142 CTD measured salinity to a nominal accuracy of 0.03 (better in regions of weak vertical gradients) and temperature to 0.001 C. Seaglider SG143 experienced CTD issues that introduced significantly greater noise. Accordingly, CTD data from this vehicle was thus not used in this analysis.

Chlorophyll was measured on the float, the gliders and ship CTD's using WetLabs fluorometers with excitation frequency of 470 nm and detected emission at 700nm. Data from the *R.V. Knorr* fluorometer were converted to chlorophyll using a dark offset and a gain and corrections for dependences on temperature, PAR, depth and yearday. The resulting fluorometer-derived chlorophyll concentration predicted the bottle concentrations with an accuracy of about 25%. Counts from the float were then converted to chlorophyll using the *R.V. Knorr* formulae, but with the gain and offset adjusted to best match the float calibration casts. The resulting float chlorophyll matches the bottles from both the *R.V. Knorr* process cruise and *Bjarni* deployment cruises with an error of 30-50%. The higher error for the float calibration is presumably due to the poorer quality of the float-bottle intercomparisons. Fluorometers from all 4 gliders were intercalibrated by comparing nearby profiles collected on intentional calibration casts and fortuitous encounters between platforms. Data were referenced to the fluorometer employed by *R.V. Knorr* using a gain and offset for each sensor, and then converted to chlorophyll using the *R.V. Knorr* formulae, but employing only the temperature correction.

Underway temperature and conductivity data from the engine intake of the *R.V. Bjarni Saemundsson* were adjusted for an 30 s lag in temperature and then smoothed over 300 s.

1.4 Physical Model

We use a nonhydrostatic numerical Process Study Ocean Model (PSOM) (*3,4*) set in an west-to-east periodic channel of 96 km extent in the x direction, and centered at 60°N with impermeable south and north boundaries at $y = 0$ and $y = 480$ km. The model uses a grid resolution of 1 km × 1 km in the horizontal. The upper 700 m of the ocean are represented by a stretched grid with 32 levels ranging in thickness from 2.5 m near the surface to 50 m at the lowermost level. The model is integrated numerically with a time step of 432 s and evolves the density, free-surface height, pressure, and three-dimensional velocity fields from an initial state, subject to the momentum and buoyancy fluxes applied through the boundary conditions at the surface.

1.5 Boundary Conditions

The total air-sea heat flux Q [W/m^2] is converted to a density flux, $F_\rho = -\frac{\alpha Q}{\rho_0 C_p}$, where the values for the thermal expansion coefficient of seawater $\alpha = 1.6 \times 10^{-4}$ °C^{-1} and the specific heat capacity of water $C_p = 3988$ J/Kg/°C are appropriate to the salinity-temperature range at our study site. This density flux is specified through the boundary condition $\kappa_\rho \frac{\partial \rho}{\partial z}\Big|_{z=0} = F_\rho$ (where κ_ρ is the vertical diffusivity) applied uniformly to the surface with an additive white noise perturbation of zero mean and standard deviation 0.01. Evaporation and precipitation have a relatively small effect on the density compared to temperature in this region so their effect is ignored. The wind stress τ is approximated as being constant in space and westerly $\tau^x = 0.2$ N/m^2 up to year day 70, that changing linearly in time to a constant easterly wind stress, $\tau^x = -0.1$ N/m^2 beyond year day 85 (see wind forcing below). The north-south component $\tau^y = 0$ throughout. This simplification of the wind forcing both agrees approximately with the low frequency variations in the wind (Fig. S11) and allows us to better assess the role of the more dynamically relevant up-/down-front component of wind on the restratification (*5*). The stress is applied using the boundary condition on the x-momentum equation $\kappa_\nu \frac{\partial u}{\partial z}\Big|_{z=0} = -\frac{\tau^x}{\rho f}$, where κ_ν is the vertical eddy viscosity, u is the velocity in the x direction, ρ is the density and f, the Coriolis parameter. The wind stress is uniform over the model domain, but is tapered to zero within a buffer zone that extends 48 km inward from the north and south boundaries so as to spread the Ekman up-/down-welling within this region, rather than concentrate it at the boundaries. The density surfaces are restored to horizontal within this region where affected by Ekman pumping due to the artificial boundaries. The buffer region is excluded from the analysis and model diagnostics are presented for the region between $y = 150$ km and $y = 300$ km.

The model uses the same values of diffusivity for momentum and density ($\kappa_\nu = \kappa_\rho = \kappa$), i.e. assumes a Prandtl number of 1. In the horizontal, we use a uniform horizontal eddy diffusivity/viscosity of 5 m^2/s. The vertical diffusivity for momentum, heat, and passive tracers, κ, decays exponentially with depth from a surface value $\kappa_0 = \max(10^{-3}, 0.05|\tau|)$ m^2/s (which lies between 10^{-3} and 10^{-2} m^2/s for the range of wind stress τ) according as $\kappa = \kappa_0 \exp(-z/z_M)$, where $z_M = H/4.6$. The ML depth H is taken as the depth where the density is 0.01 kg/m^3 less than the surface value directly above. Convective adjustment is used to parameterize convection when the water column density profile becomes unstable due to strong cooling or down front winds.

1.6 Biological Model

Light is modeled as $I(z) = I_0 \exp(-K_w z - K_{Chl} \int_z^0 Chl(z)dz)$. In the model, chlorophyll (Chl) is estimated from the phytoplankton, which is expressed in terms of carbon concentration, by using a constant carbon to chlorophyll ratio, γ. The photosynthetically available radiation at the surface, $I_0 = 0.43SW$, where SW is the incoming shortwave solar radiation. Phytoplankton within the actively mixed surface boundary layer is mixed on time scales that are shorter than the time scale of phytoplankton growth. Hence, for $z \leq H$, we assume that the phytoplankton is exposed to the average light over the ML depth, H. Phytoplankton P is modeled as

$$\partial_t P + \nabla \cdot (\mathbf{u}P) + \frac{\partial}{\partial z}(w_s P) + \mu P - mP = \frac{\partial}{\partial z}(\kappa \frac{\partial P}{\partial z}), \tag{1}$$

where $\mathbf{u}$ is the velocity of the fluid, w_s is the sinking velocity of phytoplankton, μ is the growth rate, m is the mortality rate, and κ the vertical diffusivity. The growth rate $\mu = \alpha I \mu_{max}\ (\mu_{max}^2 + \alpha^2 I^2)^{-1/2}$. Parameter values used for the simulation are obtained from the previously carried out variational optimization of a multi-compartment model with physical, biological and chemical observational data from this study (*6*) and are as follows: $K_w = 0.059$ m^{-1}, $K_{chl} = 0.041$ mg Chl^{-1} m^2, $\alpha = 0.0538$ m^2/w/d, $\mu_{max} = 0.536$ d^{-1}, $\gamma = 15$, $w_s = 1.2$ m/day, $m = 0.0748$ d^{-1}. In our model, we maintain a minimum seed population of phytoplankton in the ML prior to the bloom by restoring the vertically averaged value of P over the ML to 0.08 mg Chl/m^3 when it falls below.

The parameterization of K in terms of Chl is supported by the NAB08 data. Fig. S4 shows K computed from the depth decay of PAR measured on the Lagrangian float plotted against Chl computed from the fluorometer on the same float. The model relationship fits the data well, particularly considering that it is a value from the literature, not fit to these data in any way. It diverges somewhat from the data at the highest Chl values. These occur during the time that silicate limitation is occurring, and the model is no longer expected to reproduce the observations.

The chlorophyll:carbon ratio is constant at $\gamma = 15$. This value is intermediate between that diagnosed from a model in (*6*), and that measured on the *R.V. Knorr* cruise. Phytoplankton cell carbon was determined from flow cytometry and FlowCAM cell size measurements using Menden-Deuer and Lessard (*7*) equations for microphytoplankton; details of the flow cytometric cell carbon conversions be found at `http://data.bco-dmo.org/NAB08/Phytoplankton_Carbon-NAB08.pdf`. Chlorophyll was measured fluorometrically in acetone extracts, according to JGOFS protocols `http://data.bco-dmo.org/NAB08/Laboratory_analysis_report-NAB08.pdf`. While we agree that phytoplankton carbon-to-chlorophyll ratios decrease with increasing irradiance, low ratios ($\sim$ 15-30 g/g) were measured in early May for the initial period of the bloom when diatoms dominated the phytoplankton (i.e., when diatom carbon was >50% of total phytoplankton carbon). Only later in May, when picoeukaryotes dominated the phytoplankton biomass, did the carbon to chlorophyll ratio increase to greater than 50 g/g. The model does not claim to simulate this period. The Bagniewski (*6*) model, optimized to fit the observations, uses a variable carbon:chl ratio (*8*): During

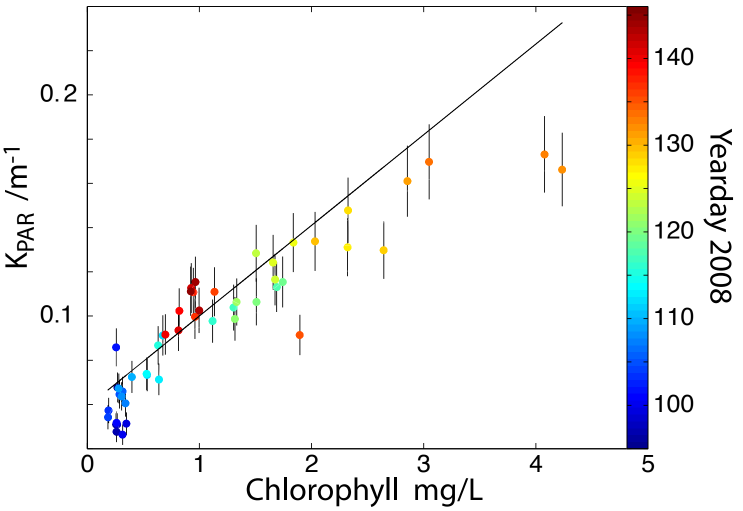

Figure S4: Scatter plot of diffuse attenuation coefficient for PAR against Chlorophyll concentration computed from fluorescence. The solid line is the relationship used in the model. Color indicates the yearday of the measurement.

the critical time of bloom growth, yeardays 110-125, the model, daily-averaged phytoplankton carbon:chl ratio varies from 8-11 in the euphotic zone.

1.7 Model Initial Conditions

The model was initialized with 3 idealized fronts running in the x (east-west) direction, (Fig. S5 left panels showing the initial x-averaged density field). The ML has 3 fronts, a north-south density gradient at the surface approximately the same as that in Fig. 1B, and no north-south density gradient at depth. The right panel, shows the x-averaged density field at day 95.5 for the NOC+25 model run. The evolution between these is shown in (Fig. S6). The initial 3 fronts go unstable and by yearday 95 are not longer apparent in the model fields. The isopycnals are now highly convoluted resulting in an average linear density gradient (Fig. S5d), which matches that measured in Fig. 1B. The average vertical ML stratification is close to the average from the Seagliders (Fig. S5f, magnenta line), but displaced upward about 200m. This compensates for the fact that the float and Seagliders were deployed into an anticyclonic eddy which depressed the pycnocline about 200 m. The array exited this feature at about yearday 110.

Spectra of model horizontal surface density gradient (Fig. S7) evolve within 20 days from the initialization (blue), with a peak at low wavenumbers, to a white spectrum falling off at wavenumbers of about 2×10^{-4} cpm (5 km wavelength). The model retains this spectral shape and level through day 100. This constant shape and level implies that an equilibrium spectrum has been achieved well before the spring bloom occurs. Observed spectra (black) have a re-

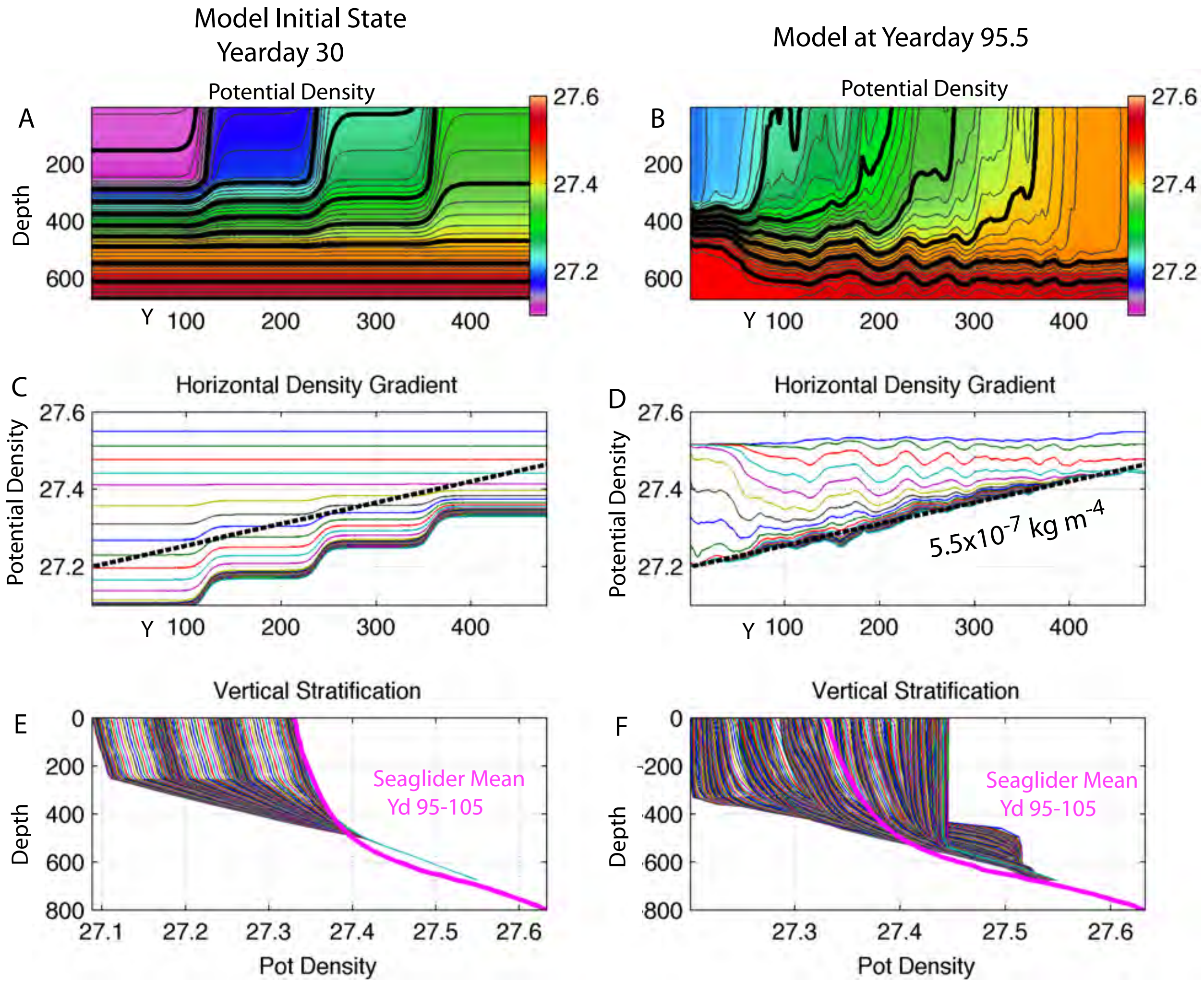

Figure S5: Model density field at model initiation (left) and at day 95.5 (right) for the NOC+25 model run. The results are nearly identical for the NOC+40 run. Top panels: colors and contours showing x-averaged potential density as function of depth (z) and north-south distance (y). Middle panels: Potential density plotted at constant depths as a function of y. The top lines are the deepest. Heavy dashed line is the potential density fit in Fig. 2B. Bottom panels: Potential density plotted at constant y as a function of z. Magenta line is the average density profile for Seagliders from days 95 to 105.

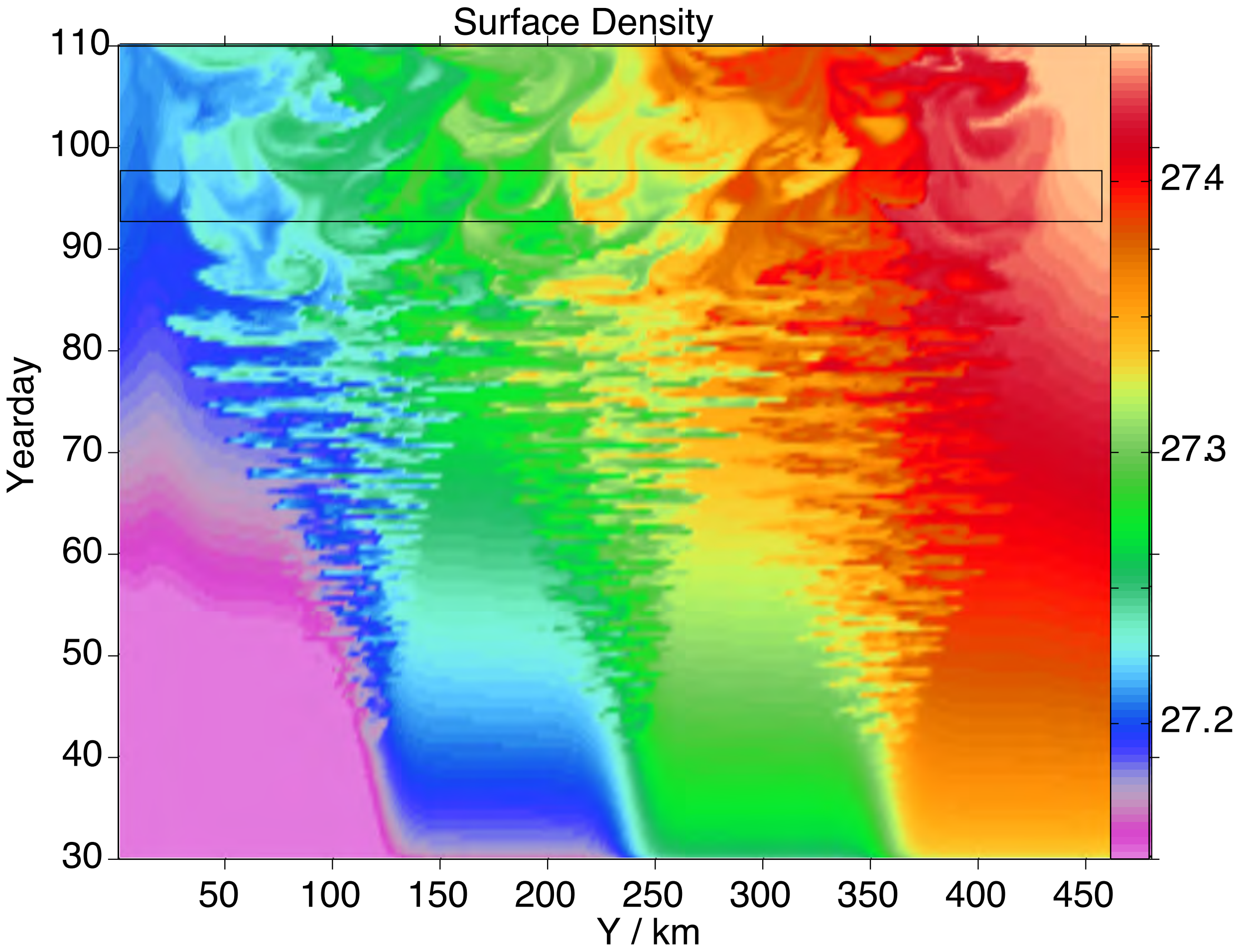

Figure S6: Evolution of surface density (color) along center of domain in model run NOC+25 as a function of time and Y distance. Light lines show time window for comparison with data.

markably similar shape, but fall off at about twice the wavenumber. Accordingly, the variance $< b_y^2 >$ is about 50% higher in the observations than in the model. To account for this, a low-passed version of the observations was constructed; the spectra of these are shown by the heavy gray lines.

Probability distributions of density gradient (Fig. S8) also evolve to a near equilibrium within 20 days. Straining of the initial gradients by ML eddies increases the rms gradient from the initial value. Observed (black) and model (colored) PDFs have a similar shape, but the observed PDFs extend to higher gradients before decreasing, consistent with the higher wavenumbers in their spectra. The low-passed observations (heavy gray lines) are much closer to the model output.

Figures S5, S7 and S8 show that the mean gradient, spectra and PDFs of density gradient from the model agree remarkably well with observations taken as the restratification was beginning. This is particularly true if the observations are weakly low-passed to reduce the highest wavenumbers. It seems likely that a modest increase in model resolution would result in a nearly perfect agreement between model statistics and the observations. Recent results from Fox-Kemper (*9*) allows the effect of this reduced model resolution to be estimated. For models with slightly underresolved fronts, they suggest increasing the ML eddy buoyancy flux by a factor $(1 + \Delta S/L_f)$ where ΔS is the model resolution and L_f is the frontal width taken as the maximum of the mixed layer Rossby number $L_R = NH/f$ and 5 km. Using representative values for NAB08, $N = 10^{-3}s^{-1}$, $H = 300\ m$ and $f = 1.2 \times 10^{-4}s^{-1}$, $L_R = 2.5$ km. For ΔS= 1 km, the flux should therefore be increased by 20%. This small increase in restratification rate is less than the uncertainty due to other factors and, if applied, would marginally improve the agreement with the observations.

We conclude that the model initiation produces fields sufficiently close to those in the ocean that the differences are unimportant to our results.

1.8 Model Forcing: Air-Sea Fluxes

Air-sea fluxes used to drive the model (Fig. 3D) and interpret the data were estimated using a combination of climatological data, model products and observations during NAB08. Three different sources are compared in Fig. S9:

(i) The "NOC" 1.1a climatology (*10*) extracted from `http://osprey.bcodmo.org/project.cfm?flag=view&id=102&sortby=project` at 60.5N 23.5W, close to the center of the NAB08 observations. It was generated from air-sea flux observations and then tuned to match an ocean model.

(ii) The "ARGO" heat flux ((*11*) their Figure 9, right, red curve), uses ARGO float data from the Icelandic Basin for 2001–2007 to infer a climatological heat flux. The NAB08 data is in approximately the center of the region of analysis. Errors are estimated at $\pm 20\mathrm{Wm}^{-2}$.

(iii) The "WHOI-OA" fluxes (*12*), which objectively combine a variety of data and model sources to compute optimal sensible and latent heat flux maps globally, are extracted for 2008 at 60.5N 23.5W. Longwave and shortwave radiation at the surface are taken from ISCCP (*13*).

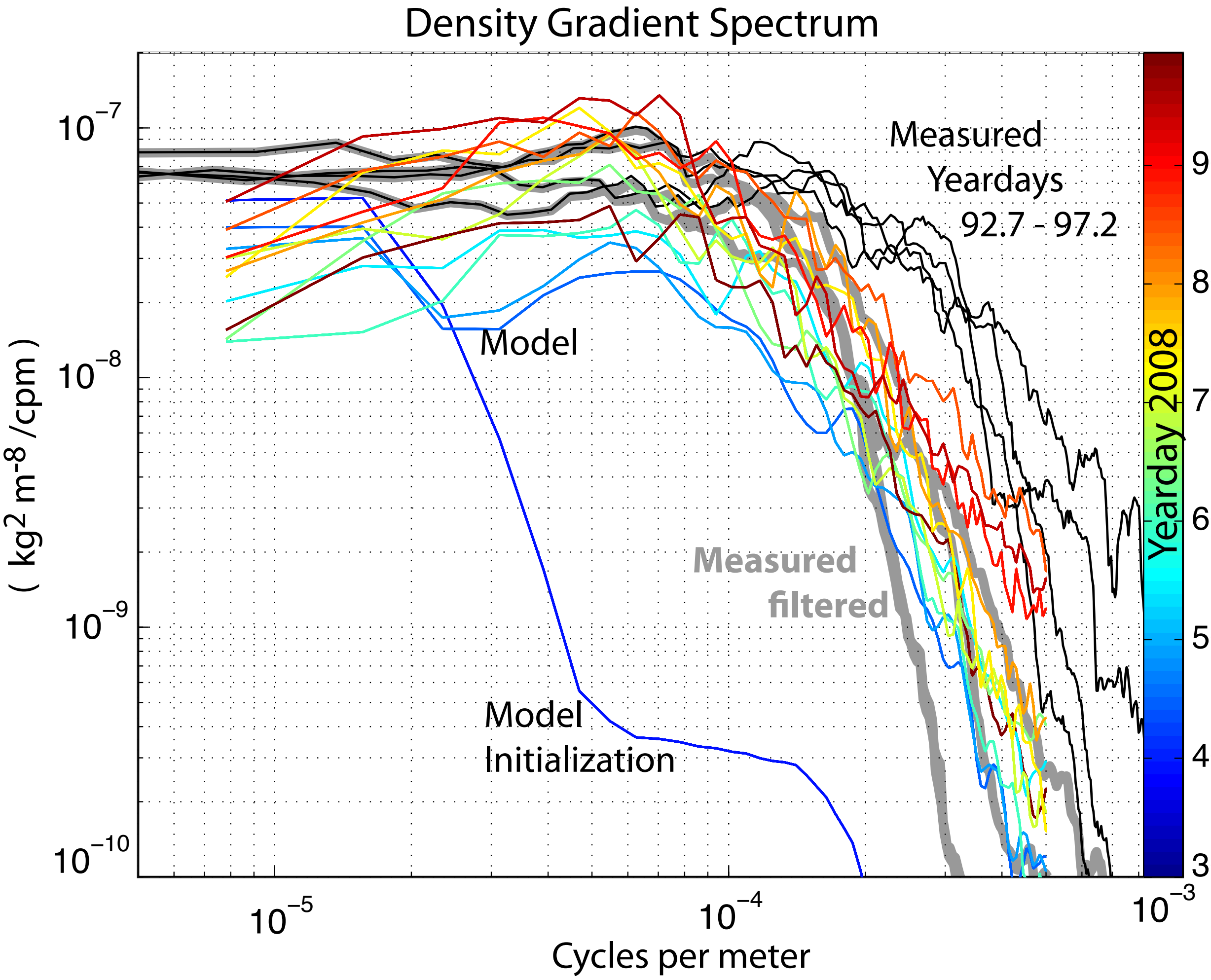

Figure S7: Horizontal wavenumber spectrum of density gradient from model (colors) and observations along the ship track in Fig. 1b (black). Color indicates time. Model spectra are averaged over 5 days; selected spectra concentrated near day 85-100 are shown. Observed spectra (black) are from four, approximately 250 km-long, segments. Spectra of the same data, but low-pass-filtered to better match the model spectra are shown by thick gray lines.

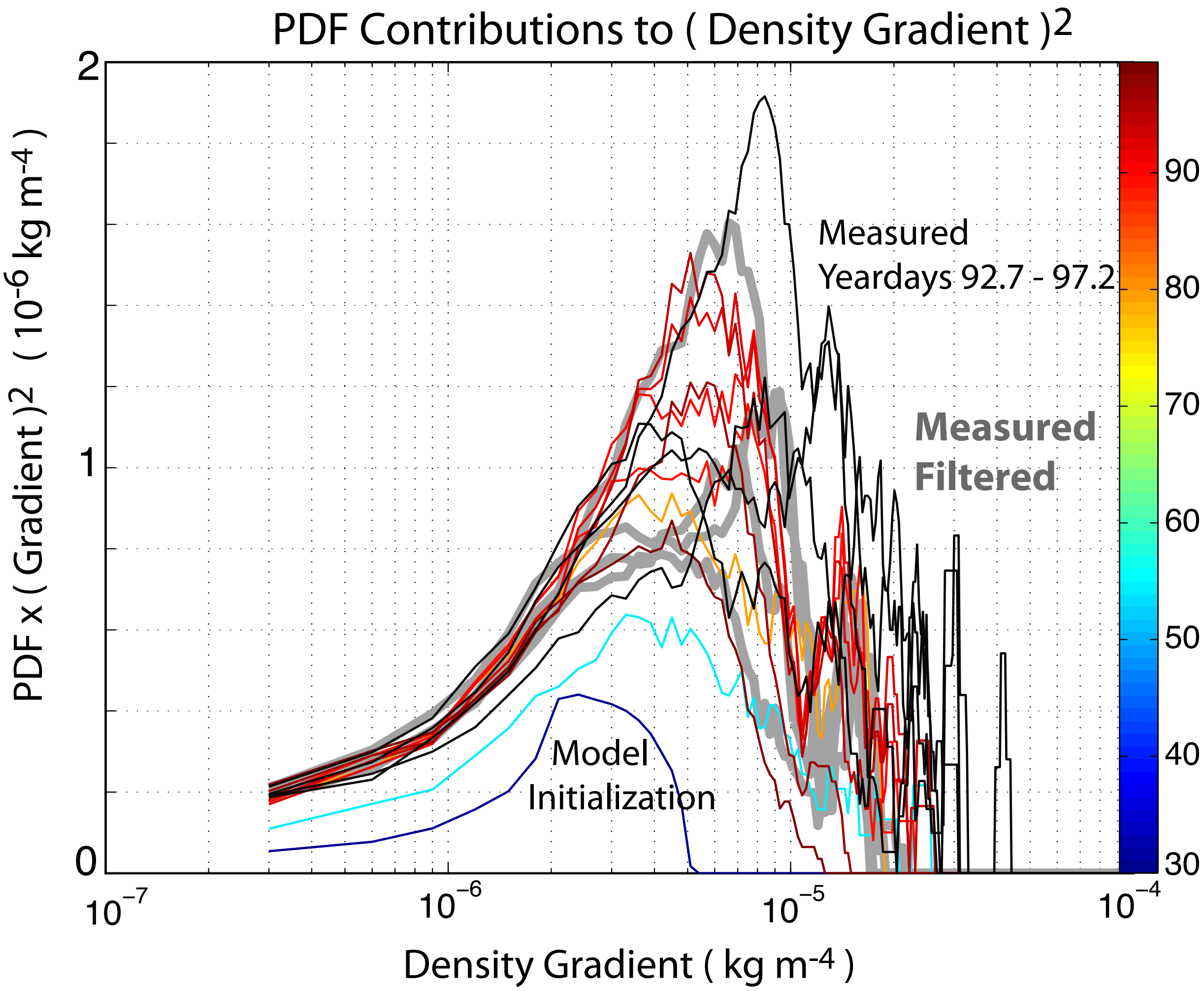

Figure S8: Probability distribution (PDF) of horizontal surface density gradient from model (colored) and observations (black). For a PDF $P(b_y)$ normalized so that $\int P(x)dx = 1$, the squared density gradient is given by $< b_y^2 >= \int x^2 P(x)dx$. Here $b_y^2 P(b_y)$ is plotted. This emphasizes the long tails that dominate the contribution to $< b_y^2 >$. Model PDFs are averaged over 5 days; selected PDF's concentrated near day 85-100 are shown. Observed PDF's (black) are from $4 \approx 250$ km-long segments. PDFs of the same data, but low-pass-filtered to better match the model spectra are shown by thick gray lines.

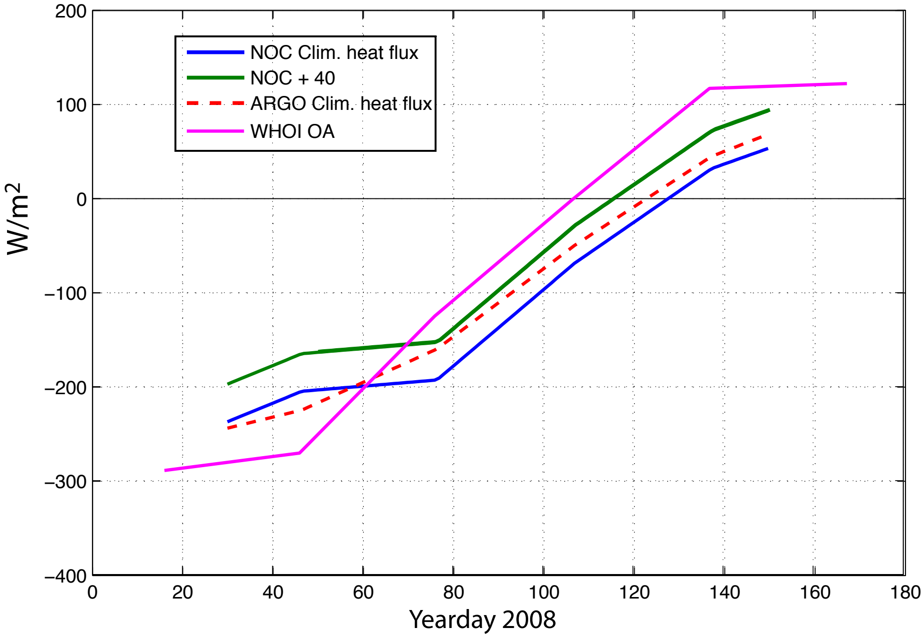

Figure S9: Total surface heat flux estimates from various products at the NAB08 site

Monthly average data is extracted from 60.5N 23.5W. Errors for the two turbulent components are estimated at $\pm 6\mathrm{Wm}^{-2}$ each from the objective analysis. The ISCCP errors are larger $\pm 18\mathrm{Wm}^{-2}$ for the two radiative components over the latitude band of our observations. Summing these errors yields $\pm 48\mathrm{Wm}^{-2}$; summing the squares and taking the square root yields $\pm 27\mathrm{Wm}^{-2}$. These estimates are standard deviations so the 95% errors are closer to $\pm 54\mathrm{Wm}^{-2}$.

The NOC fluxes are the smallest, about $20\,\mathrm{Wm}^{-2}$ below ARGO. The WHOI-OA 2008 fluxes are about $50\,\mathrm{Wm}^{-2}$ larger (Fig. S9). In particular, the ARGO and NOC fluxes only become positive on about day 125, while the WHOI-OA fluxes become positive around day 105. This has important implications for the timing of the bloom.

Fig. S10 compares the evolution of the ML temperature at the Lagrangian float with that predicted from the various heat flux products. The ML depth is chosen as the depth at which the potential density is $0.005\,\mathrm{kg\,m}^{-3}$ larger than the shallowest value for each daily float profile. Daily values are filtered with a 3 day running median and smoothed over about a day. The change in ML temperature due to surface heat fluxes is estimated by distributing the surface heat flux over this layer and integrating to get the change over time. NOC lies below the ML temperature, ARGO lies near it, NOC+40 lies above it, and the 2008 WHO-OA fluxes are far above it. Thus NOC and NOC+40 span the observed change in ML temperature while each being within the range of error for ARGO. We thus use NOC and NOC+40 to represent the range of heat fluxes.

Interannual variability was investigated using the WHOI-OA fluxes for 2000-2009. The year 2008 was within $20\,\mathrm{Wm}^{-2}$ of the average flux for all years during March and April, but

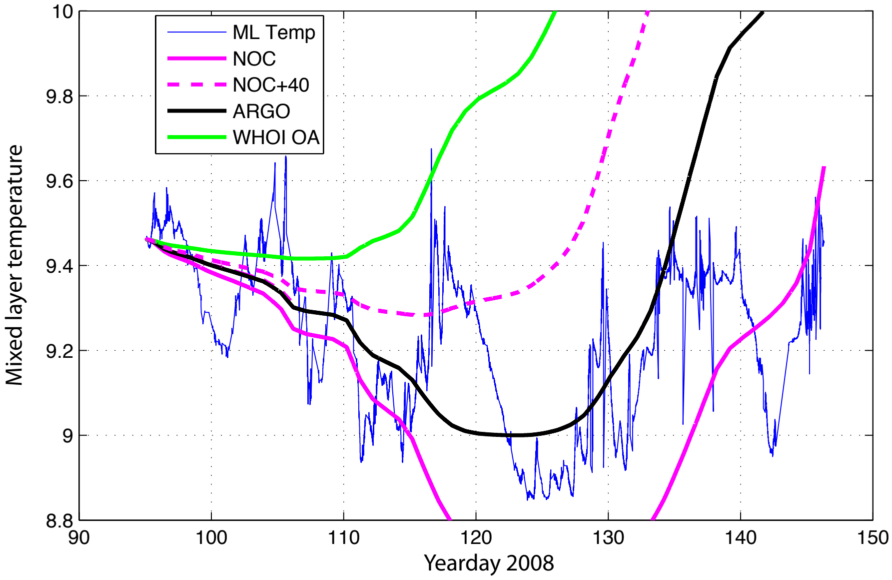

Figure S10: ML temperature from the Lagrangian float and that computed by integrating the various heat flux products.

$\sim 30\,\mathrm{Wm}^{-2}$ above the mean for May (yeardays 122-152). Thus although we are using a climatological product to analyze data from 2008, the year 2008 appears to be close to climatology for the months of March and April during which the bloom initiation occurs, only deviating for May, after the time where ML eddy restratification is important.

We use a north-south gradient in heat flux, with a difference of $50\,\mathrm{Wm}^{-2}$ over the 500 km domain, which is about 60% above the estimated meridional heat flux gradient in the NOC 1.1a climatology. This density gradient primarily serves the purpose of maintaining the north-south density gradient against the diffusive effects of the ML eddies. In the real ocean this is additionally accomplished through lateral advection, so adding a small additional flux gradient seems appropriate. Results of the simulations are not sensitive to this value within this range.

Surface shortwave radiation for photosynthesis is taken from the shortwave radiation estimate from NOC 1.1a. No north-south gradient in shortwave radiation is used as the gradient in the NOC 1.1a is small.

Additional comparisons with the NOC heat flux were made using underway data from the *R.V. Knorr* cruise on days 122-142. Sea surface temperature data was adjusted by 0.11 C to match the float temperature data. Other sensors were not recalibrated. Turbulent and shortwave fluxes were computed as implemented in the hfbulktc() and swhf() functions of the Matlab Air-Sea toolbox `http://woodshole.er.usgs.gov/operations/sea-mat/air_sea-html/index.html`. Longwave fluxes were computed using the blwhf() and cloudcor() functions. The various options of these functions result in changes of only a few Wm^{-2}. The average air-sea heat flux for days 122-142 is $26\mathrm{Wm}^{-2}$ (warming) with an error of at least

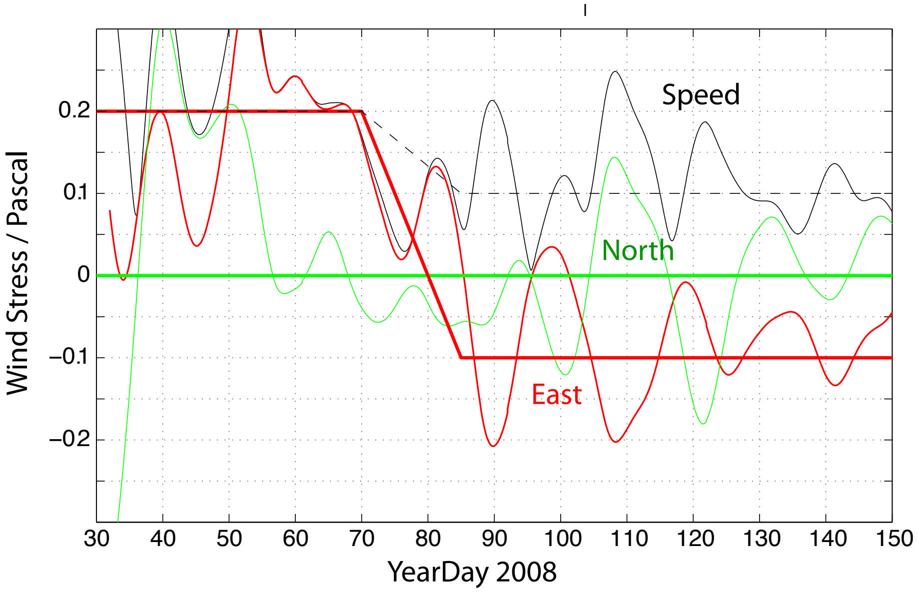

Figure S11: Wind Stress Components and Magnitude from NOAA Wave Watch 3, smoothed (thin lines) and idealization used to drive model (thick lines)

$10\mathrm{Wm}^{-2}$. These are plotted in Fig. 3D and verify that our heat flux estimates are reasonable.

Winds (Fig. S11, Fig. 3E) were estimated from the Wave Watch 3 model run by NOAA `http://polar.ncep.noaa.gov/waves`. The 3-hourly data was interpolated to the location of the Lagrangian float. Wind stress is computed from these winds using a neutral (*14*) drag coefficient and smoothed with a 8.3 day Butterworth filter. The solid lines in Fig. 3E, used to drive the model, were chosen by eye.

1.9 Model Simulations

The model is run for 120 days starting from year day 30. During the initial period, cooling is strong and vertical mixing deepens the ML, keeping the isopycnals vertical even as the density fronts in the ML become baroclinically unstable, In the resulting eddying flow field (Fig. S12), the vorticity attains values as large as the planetary vorticity f, particularly in filaments, indicative of submesoscale processes. Fig. S13 shows the density structure in the model prior to the onset of stratification (yearday 90) and soon after stratification has set in (yearday 120).

The restratifying tendency of the ML eddies is countered by cooling and downfront winds, which transport heavier over lighter water at the surface and induce convection near the fronts. Though the model is nonhydrostatic, the grid spacing is not fine enough to resolve convective plumes. Convective adjustment is run with a fixed number of iterations per time step; hence some negative stratification develops in the model close to the surface during the time when cooling is strong and the winds are downfront. When the wind switches direction to upfront,

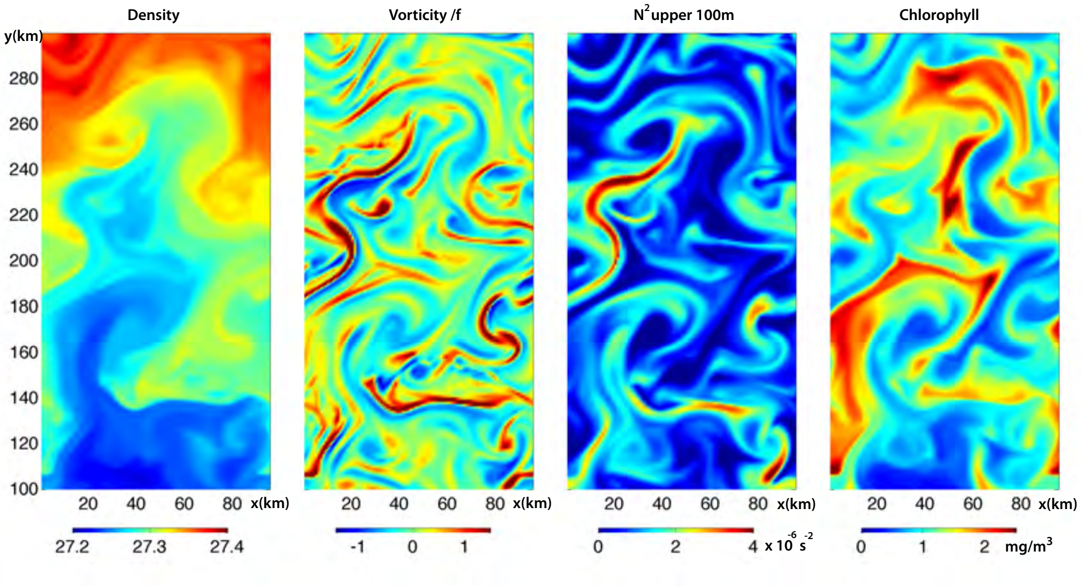

Figure S12: Yearday 118 from the model simulation showing (a) density at 6 m depth, (b) vertical component of relative vorticity at 6 m depth normalized by f, (C) N^2 averaged over the upper 100 m, and (d) chlorophyll at 6 m depth, soon after the onset of the spring bloom. The vorticity is maximum in the regions of largest horizontal density gradients, and is larger than f in many places as the ML eddies are submesoscale in character. N^2 is also enhanced most in regions of strong lateral density gradient due to the slumping of isopycnals. Chlorophyll growth rates are maximum in regions of shallow stratification, but the chlorophyll itself integrates this effect in time.

they drive an Ekman transport of lighter water over denser water and augment the restratifying tendency of the eddies.

2 Supplementary Simulations

The model cases run are listed in Table S1. Cases 1,3,4,5 are shown in Fig. 3; the additional cases 6,7,8 are shown in Fig. S9 with case 1 (black) as a reference. Case 2 is used in Fig. S4 and S8. If the heat flux does not increase beyond $-150\,\mathrm{Wm}^{-2}$ (case 6, labeled ‘Cooling’, magenta) the ML does not restratify. If the wind does not switch from downfront to upfront (case 7, ‘Downfront wind’, blue), restratification occurs but is delayed. Finally, if there is no heat flux, and no wind forcing (case 8, ‘No Flux’, red), the ML restratifies during the entire simulation. These additional runs confirm that the ML eddies restratify the boundary layer, that this is prevented by cooling and assisted by the switch to upfront winds.

3 Supporting Equations

The strength of the mean overturning streamfunction induced by ML eddies (MLE) is given by $\psi_e = 0.06\, b_y\, H^2 f^{-1}$ (*15*). The vertical buoyancy flux due to ML eddies is $\langle w'b'\rangle_e \sim \langle \psi_e\, b_y\rangle$

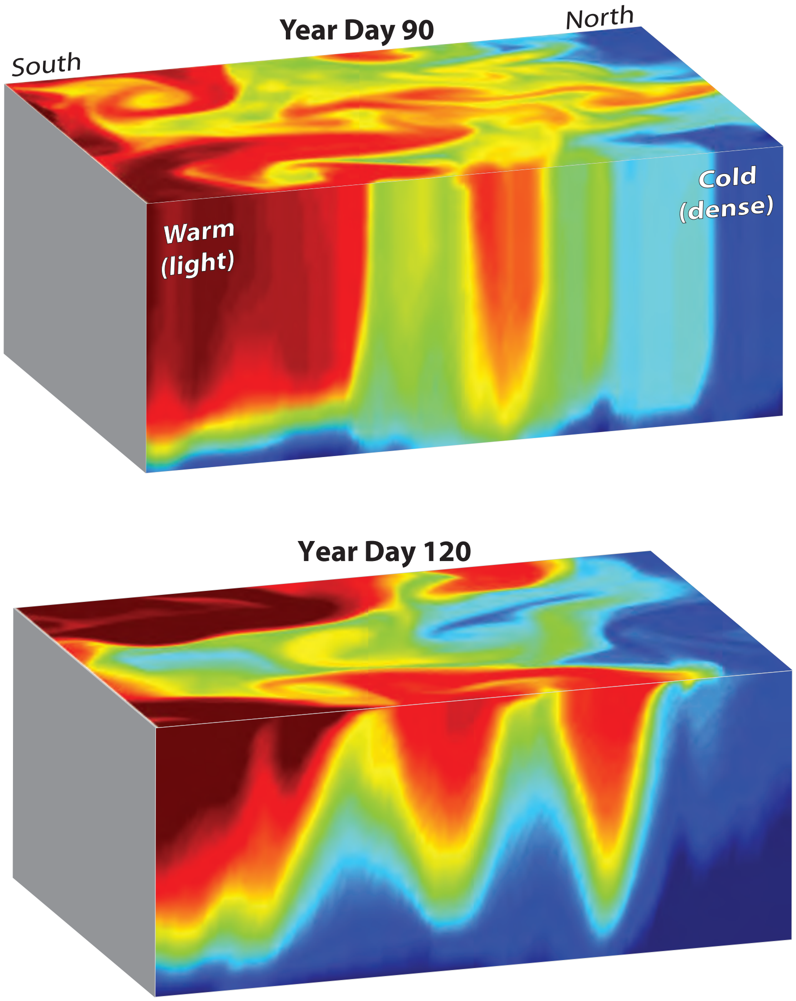

Figure S13: Density field in the model shown (a) at year day 90, prior to the onset of stratification, and (b) on year day 120, after stratification has set in. Density ranges from 27.27 kg/m^3 to 27.4 kg/m^3 between the deepest red and blue shades in the figure. In (a), strong cooling and down front winds keep the surface layer well mixed and, even though an active eddy field is developed, density surfaces are vertical within the ML. In (b), cooling is very weak, and the ML eddies have slumped the isopycnal surfaces, converting horizontal density gradients to vertical density gradients within the ML. The regions where the ML has shoaled provide more light exposure to phytoplankton and are the regions that support maximal phytoplankton growth.

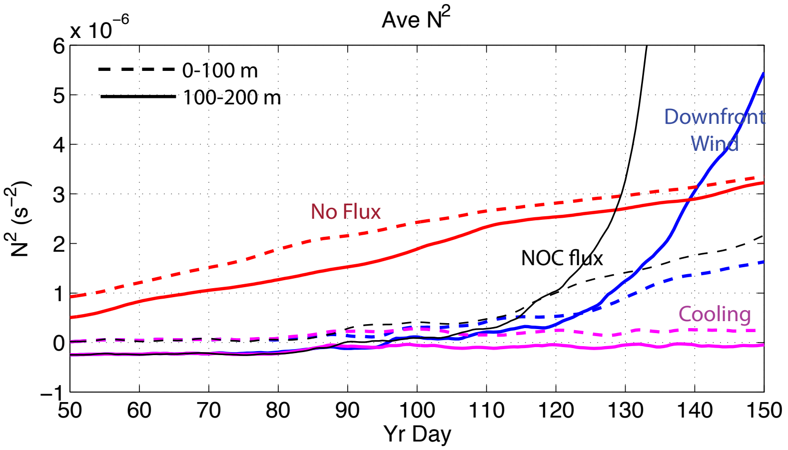

Figure S14: Average stratification, N^2, in the upper 100 m and 100–200 m for the baseline simulation with NOC fluxes (Black) is compared with case 6 (magenta), 7 (blue) and 8 (red) as described in Table S1.

Case	Initial condition	Heat flux Q	Meridional ΔQ	Wind stress
1	Fronts	NOC	50 w/m^2	Down-/up-front
2	Fronts	NOC + 25 w/m^2	50 w/m^2	Down-/up-front
3	Fronts	NOC + 40 w/m^2	50 w/m^2	Down-/up-front
4	No fronts	NOC	0	Down-/up-front
5	No fronts	NOC + 40 w/m^2	0	Down-/up-front
6	Fronts	min(NOC,-150 w/m^2)	50 w/m^2	Down-/up-front
7	Fronts	NOC	50 w/m^2	Down-front 0.2 N/m^2
8	Fronts	0	0	0

Table S1: Configurations of model simulations.

where $\langle\cdot\rangle$ denotes the along-front average.

The vertical buoyancy flux due to cooling $\langle w'b'\rangle_{cool} = -\frac{\alpha Q g}{\rho C_p}$ where Q is the (cooling) heat flux (watts/m^2), α is the thermal expansion coefficient (per ^{0}K), C_p is the specific heat capacity of sea water at constant pressure (J/kg/^{0}K), and ρ is the density of seawater.

The vertical buoyancy flux due to a downfront wind stress, τ, induced overturning is $\langle w'b'\rangle_{wind} \sim \langle \psi_w \, b_y\rangle = \langle \frac{\tau}{\rho f} b_y\rangle$. It is worth noting that $\langle w'b'\rangle_e$ acts in the opposite (restratifying) sense to $\langle w'b'\rangle_{cool}$ and $\langle w'b'\rangle_{wind}$, which are destratifying.

In our experiments, $b_y = -0.3 \times 10^{-7}$ s^{-2} at each of the fronts, H=300 m, $f = 1.28 \times 10^{-4}$ s^{-1}, $\alpha = 1.6 \times 10^{-4}$ K^{-1}, $C_p = 3988$ J/kg/^0K.

What rate of cooling is needed to keep the front from restratifying? Equating $\langle w'b'\rangle_{cool}$ to $\langle w'b'\rangle_e$ gives $Q = 0.06\frac{b_y^2\,H^2}{f}\frac{C_p \rho}{\alpha g} = -100$ watts/m^2.

What downfront wind stress will keep the front destratified? Equating $\langle w'b' \rangle_{wind}$ to $\langle w'b' \rangle_e$ gives $\tau = 0.06 \rho b_y H^2 = 0.15$ N/m^2, in the absence of cooling. The down-front wind becomes misaligned with the front as it begins to meander. So when the front becomes unstable, it begins to restratify initially, the ML eddies consequently weaken, and the mean effect of the wind arrests further restratification.

4 Patchiness in Chlorophyll

Figure S15 compares spectra of Chlorophyll from the model and from the one good MODIS image in the NAB08 region during the time of rapid bloom growth. This image is about 150 km east of the NAB08 platforms at the same time. Both model and data spectra are white near 100 km wavelength, and decay to approximately -2 slope to about 10 km wavelength. Below this, the model spectra drop more rapidly (Fig. S7) as the model resolution is approached. The MODIS spectra flatten, presumably due to an instrumental noise floor. The heavy line in Fig. S15 subtracts a constant spectral noise in an attempt to compensate. The model spectra change somewhat in shape over time, being slightly whiter near yeardays 70-80 and steeper after day 100. Additional uncertainty in the data spectra is introduced by the relatively small domain, which is unlikely to capture all of the variability in chlorophyll in this region. Bearing this in mind, the similar shapes of the model and data spectra indicate that the model is capturing the distribution of patchiness scales in the data.

Figure S16 examines the spatial correlation between stratification and chlorophyll during the period of rapid bloom growth. Since both chlorophyll and stratification are increasing during this period, a strong temporal correlation exists between them. This is removed by fitting exponential curves (Fig. S16ab). The residuals show a weak correlation (Fig. S16c). Assuming independence of each glider profile, this is highly statistically significant. Adjacent profiles of Chl/Chl_{fit} and N^2/N^2_{fit}, i.e. n and $n+1$ are correlated, and thus not completely independent. This correlation drops below 0.3 for profiles n and $n+2$, and remains significant at the 0.4% level if only every other profile is used.

5 Alternative Hypotheses

5.1 Relaxation of Turbulence

An alternate hypotheses (*16*) suggests that a suppression of active turbulence in the mixed layer can generate a bloom. Fig. S17 (upper panel) shows the rms vertical velocity experienced by the Lagrangian float within the mixed layer. No decrease in rms vertical velocity is observed in association with the bloom initiation. The hypothesis also requires strong gradients of chlorophyll within the mixed layer. No such gradients are seen (lower panel).

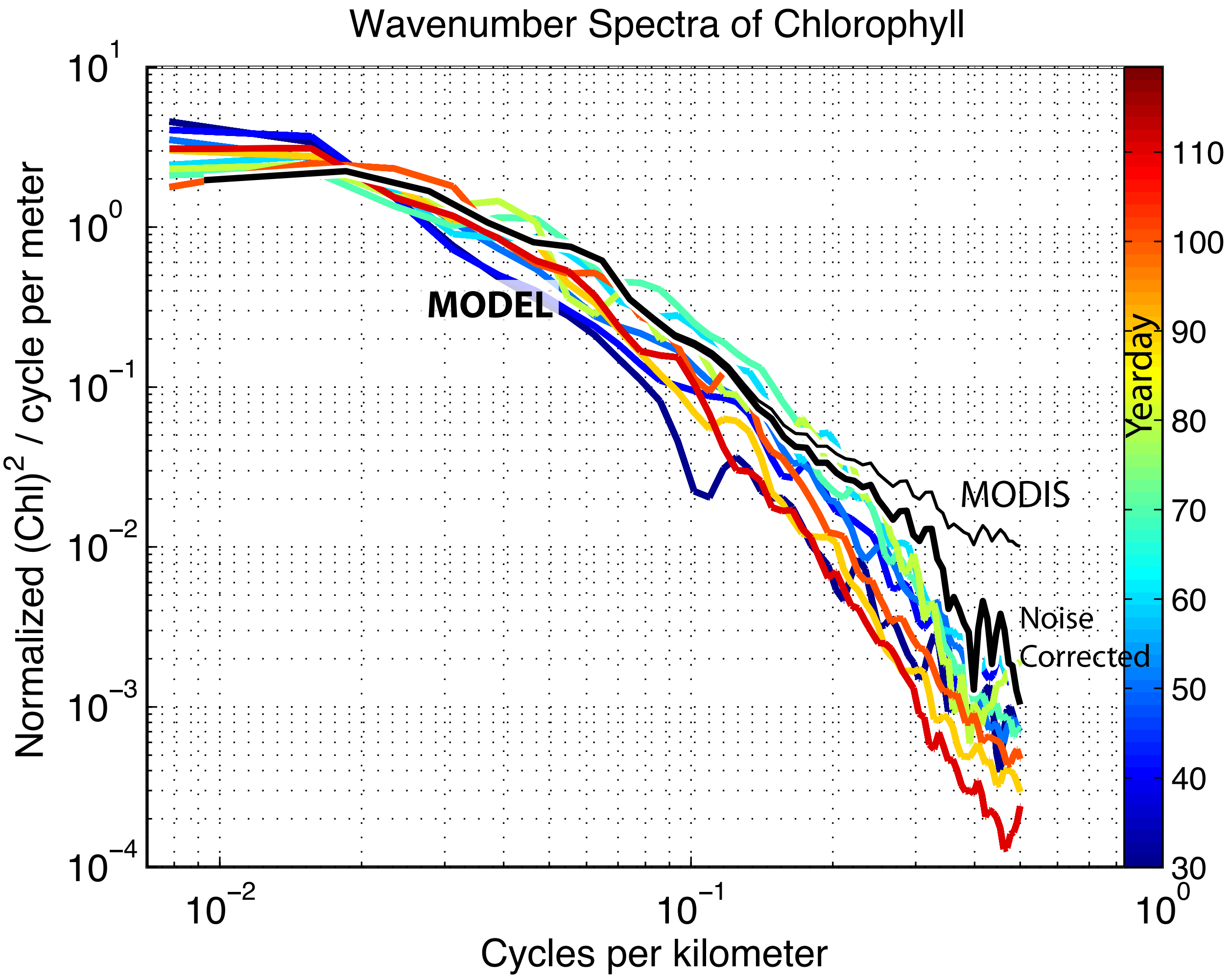

Figure S15: Spectra of Chlorophyll (colored) and boxed region of Fig. 4B. Model Chlorophyll from north-south lines in NOC+25 model run are averaged over 20 days and colored by day. Data spectra from east-west lines of Fig. 4B with a small number of data gaps linearly interpolated is shown by light black line. A noise corrected spectrum is shown by the heavy black line. All spectra are normalized by the mean of the spectral levels below 1 cpkm.

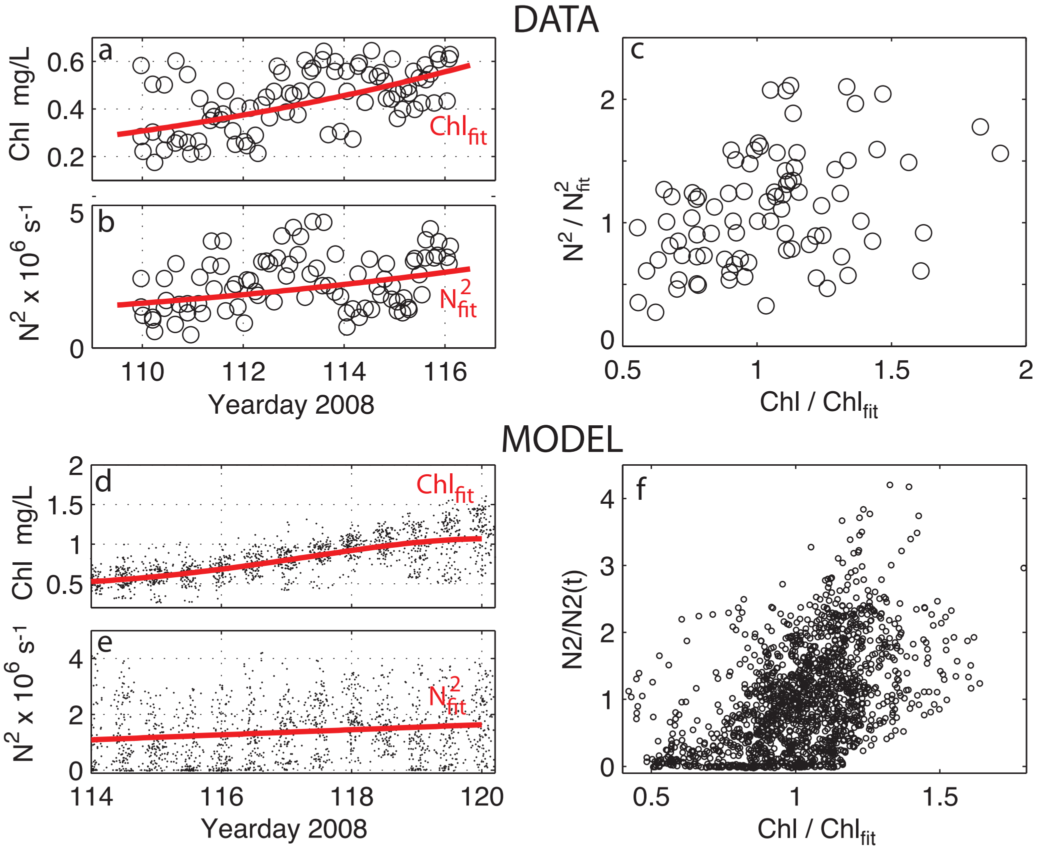

Figure S16: (a) Average chlorophyll (10-100 m) from gliders (140, 141 and 142) during rapid growth of bloom. Red line shows exponential fit Chl_{fit} (b) Average stratification N^2 from linear fit to the same glider data. Red line shows the fit N^2_{fit} c) Scatter plot of Chl/Chl_{fit} and N^2/N^2_{fit}. Correlation (r=0.39) is significant at the 0.02% level assuming independent measurements in each profile and at the 0.4% level if only every other point is used. d-f) Same but for NOC+25 model run. Using model output points 10 km apart, clearly independent based on the autocorrelation function, the correlation (r=0.53) is highly significant.

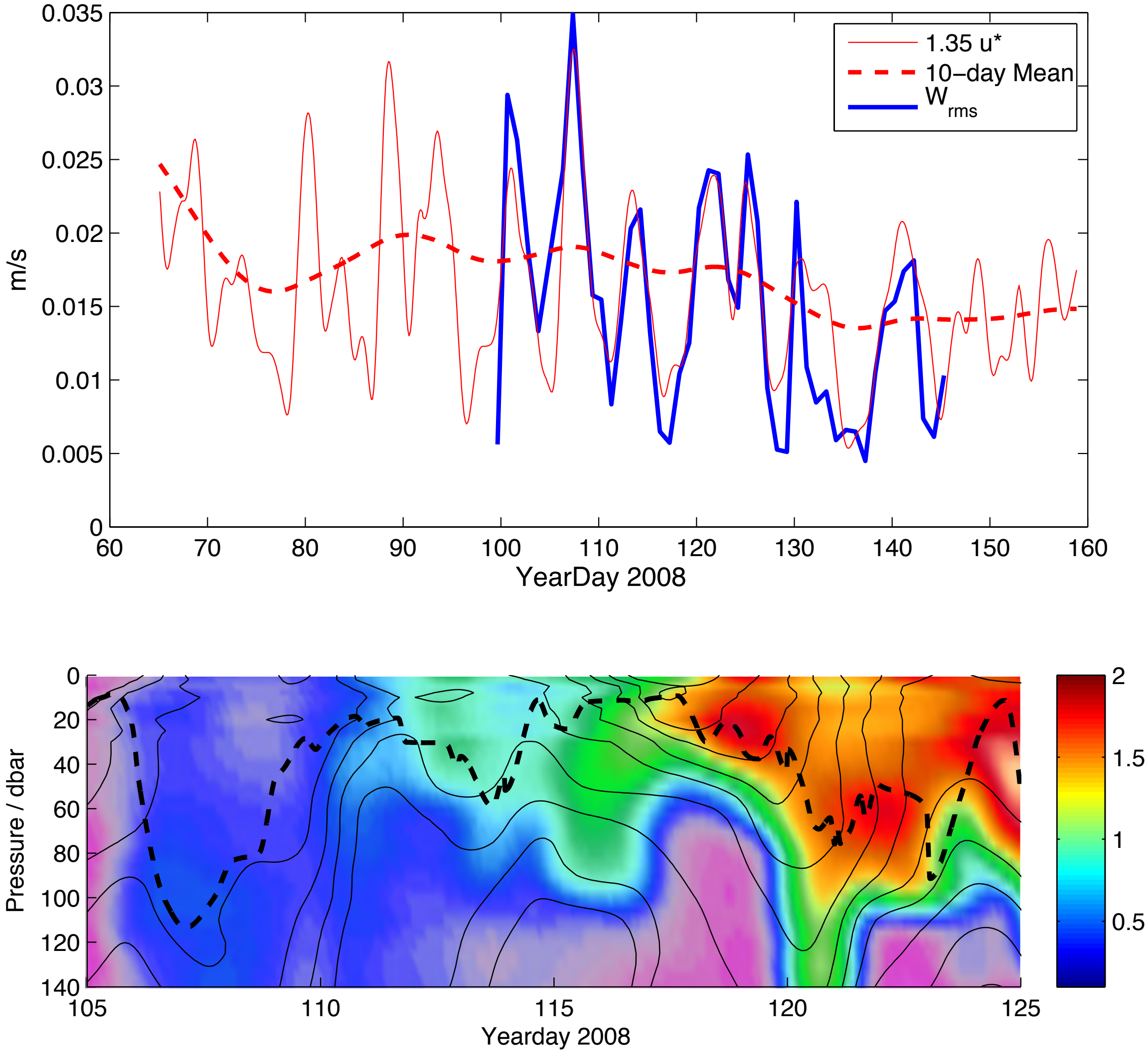

Figure S17: (Upper) Daily average rms vertical velocity measured by the Lagrangian float within the mixed layer (blue). This is highly correlated with the wind stress. w_{rms} estimated from daily smoothed wind stress (thin red) and 10 day smoothed wind stress (thick dashed red) are shown. None of these show a reduction in mixing when the bloom starts. (Lower) Chlorophyll mapped from the Lagrangian float observations. Dashed line is the mixed layer depth. No surface increase in Chlorophyll is seen within the mixed layer.

5.2 Symmetric instability

Another hypothesis is that Symmetric instability (SI) (*17*), not ML eddy restratification causes the restratification . SI acts to convert a lateral buoyancy gradient to a vertical gradient when that lateral gradient is large enough, and vertical gradient weak enough that the potential vorticity is negative.

Consider a region of size L with a lateral buoyancy gradient of $M^2 = b_y$ and a vertical stratification of $N^2 = b_z$ for buoyancy $b = -g\rho/\rho_0$ for density ρ, gravity g and reference density ρ_0. The potential vorticity is

$$Q = (f\hat{k} + \zeta) \cdot \nabla b \tag{2}$$

for relative vorticity ζ. This can be written as

$$Q = (f + \chi)N^2 + U_z M^2 \tag{3}$$

where χ is the vertical vorticity and U_z, the y-horizontal vorticity, is the vertical shear of velocity U.

SI can only occur for $Q < 0$, with second term in (2) negative, or $N^2 < U_z M^2/(f + \chi)$. If L is sufficiently large that the flow is geostrophic $U_z = M^2/f$ and $\chi/f << 1$, then SI can occur only if

$$N^2 < M^4/f^2 \tag{4}$$

Applying this to the Icelandic Basin case $M^2 = 5 \times 10^{-9} s^{-2}$, $f = 1.2 \times 10^{-4} s^{-2}$, so $N^2 < 1.7 \times 10^{-9} s^{-2}$, many orders of magnitude below the observed stratification. Thus SI cannot be responsible for creating these large stratifications on this large scale.

6 Supplementary Movie

Attached File: MahadevanSuppMovie.mov
Supp. Movie 1: An animation of our model simulation showing the time evolution of density and chlorophyll within a sub-region that spans the central one-third of the north-south extent of the domain (y=161-320 km, x=0–96 km). The full model domain (y=0–480 km) has multiple fronts; we focus here on just one portion for clarity. The model is run from initialization at yearday 30 until yearday 150, results are shown up to yearday 130 beyond which, the model chlorophyll is saturated because nutrient (silicate) limitation is not considered.

The top row shows near surface (6 m depth) density and chlorophyll. The plots are oriented with north to the right and west toward the top. Blue colors indicate cooler, denser water, red indicates warmer, lighter water. The color scale for chlorophyll is logarithmic.

The second row shows vertical cross sections of density and chlorophyll in the upper 320 m, centered midway between the periodic east-west boundaries. White lines denote isopycnals and the thick grey line denotes the depth of the mixed layer (ML) estimated as the depth where the density exceeds the surface value by 0.01 kg/m^3.

The lowest row shows the time dependent forcing: wind stress, heat flux and incoming shortwave radiation. Positive wind stress indicates westerly, down-front winds. This simulation uses the NOC heat flux +40 w/m^2.

In approximately 30 days, the initial fronts develop into an eddying flow field. While cooling is strong and winds are down-front (westerly), the eddies, though active, are unable to stratify the ML. After day 95, a weakening in the cooling rate, coupled with up-front winds, enables the eddies to begin restratifying the surface ML. Chlorophyll is seen to develop in shallow pockets overlying the restratified regions.

ERATA The version in ScienceMag has a minus sign missing on the exponent 1/2 in the formula for growth rate.

References

1. C. Eriksen, *et al.*, *Oceanic Engineering, IEEE Journal of* **26**, 424 (2001).
2. E. A. D'Asaro, *J. Atmos. Ocean. Technol.* **20**, 896 (2003).
3. A. Mahadevan, J. Oliger, R. Street, *J. Phys. Oceanogr.* **26**, 1168 (1996).
4. A. Mahadevan, *Ocean Modelling* **14**, 222 (2006).
5. A. Mahadevan, A. Tandon, R. Ferrari, *J. Geophys. Res.* **115** (2010).
6. W. Bagniewski, K. Fennel, M. J. Perry, E. A. D'Asaro, *Biogeosciences* **7**, 1 (2010).
7. S. Menden-Deuer, E. J. Lessard, *Limnol. Oceanogr.* **45**, 569 (2000).
8. R. J. Geider, H. L. MacIntyre, T. M. Kana, *Mar Ecol Prog Ser* **148**, 187 (1997).
9. B. Fox-Kemper, *et al.*, *Ocean Modelling* **39** (2011).
10. J. P. Grist, S. A. Josey, *Journal of Climate* **16**, 3274 (2003).
11. E. de Boisséson, V. Thierry, H. Mercier, G. Caniaux, *J. Geophys. Res.* **115** (2010).
12. L. Yu, R. Weller, *Bull. Amer. Meteor. Soc.* **88**, 527 (2007).
13. Y. Zhang, W. B. Rossow, A. A. Lacis, V. Oinas, M. I. Mishchenko, *J. Geophys. Res.* **109**, D19105 (2004).
14. W. Large, S. Pond, *J. Phys. Oceanogr.* **11**, 324 (1981).
15. B. Fox-Kemper, R. Ferrari, R. Hallberg, *J. Phys. Oceanogr.* **38**, 1145 (2008).
16. J. Taylor, R. Ferrari, *Geophys. Res. Lett.* **38**, L23601 (2011).
17. J. Taylor, R. Ferrari, *Limnol. Oceanogr.* **56**, 2293 (2011).